Local Crippling of Thin-Walled Graphite-Epoxy Stiffeners

David L. Bonanni*
David Taylor Research Center, Bethesda, Maryland 20034
and
Eric R. Johnson†
Virginia Polytechnic Institute and State University, Blacksburg, Virginia 24061
and
James H. Starnes Jr.‡
NASA Langley Research Center, Hampton, Virginia 23665

Results from an experimental and analytical study of the local buckling, postbuckling, and crippling (failure) behavior of channel, zee, and I- and J-section stiffeners made of AS4/3502 graphite-epoxy unidirectional tape are presented. Thirty-six specimens were tested in axial compression. Experimental results indicate the existence of a number of damage-initiation modes, all of which involve either delamination in some part of the specimen or local material strength failure in a corner of the specimen. The flange width-to-thickness ratio is found to influence the mode of damage initiation. The inner corner radius strongly affects the crippling stress for the I- and J-section specimens, but was not found to have a significant effect on the crippling stress of channels and zees. Geometrically nonlinear analyses of five specimens were performed with the STAGS general-purpose computer code. Correlation between analytical and experimental results is excellent through buckling, but agreement degrades in postbuckling. The discrepancies in postbuckling are attributed to the neglect of transverse shearing deformations in the analysis and development of damage in the specimens. The maximum compressive fiber stress-failure criterion correlates reasonably well with the first major damage event observed in the tests.

Introduction

THE compression strength of thin-walled semimonocoque of structures is often governed by a local buckling instability with a subsequent failure during the postbuckling response. Local buckling of a thin-walled stiffener is characterized by bending deformations of the flange and web elements, similar to the bending of individual plates restrained along one or both unloaded edges, while the junctions between flanges and webs remain relatively straight and parallel. It is possible for such stiffeners to support compressive loads greater than the local buckling load because of the mutual rotational restraint exerted by cross-sectional elements meeting at a common junction. Eventual failure of a stiffener in the postbuckled state is called local crippling, and usually precipitates failure of the stiffened structure.

Because of the bending deformation of the flange and web elements of a buckled stiffener, the increased compression in postbuckling is largely carried by the junctions, or corners, between the flanges and webs. The crippling-failure mode of metallic thin-walled stiffeners is known to be a local collapse initiated by material yielding in the corners of the section caused by this load redistribution in postbuckling. Although laminated composite materials are attractive for weight-sensitive structures, their use in postbuckled designs depends on understanding and quantifying their crippling-failure mechanisms. A particularly important difference between metals and laminated composite material system is the susceptibility of composite systems to delamination and other brittle-failure mechanisms.

Many crippling studies have been conducted on composite material stiffeners.[1-13] Spier and his co-workers[1-6] have performed extensive experimental investigations on plates, open- and closed-section stiffeners, and stiffened panels to develop semiempirical buckling and crippling curves similar to those used for metallic stiffener crippling. Experimental observations of the crippling-failure process in composite stiffeners indicate that the initiation of failure occurs either at a corner[2,7,11] or at the free edge of a flange.[7-10] Failure initiation at the corner is attributed to a local compressive strength failure[7] or delamination.[11] Failure initiation at the free edge of a flange is consistently attributed to delamination.[7-10] High-speed photography was used in Ref. 9 to find delamination initiating failure at the free edge of a flange in an I-section stiffener, followed by a local material strength failure in the web.

Arnold and Mayers[13] developed a geometrically and materially nonlinear analysis for the no-edge-free plate specimens of Ref. 6. The maximum compression fiber strain criterion predicted the theoretical crippling loads in close agreement with experimental crippling loads. Geometrically nonlinear finite element analyses of stiffeners and stiffened panels have successfully predicted postbuckling response,[11,14] but the delamination failures of the test specimens could not be predicted by these analyses since they are based on plate/shell theory.

A number of different failure modes for thin-walled composite stiffeners in compression have been documented or hypothesized in the literature. However, the establishment of crippling criteria based on the mechanisms of failure in composite material stiffeners is incomplete. This paper presents and discusses some of the results of a combined experimental and analytical study[12] that addressed this problem. The primary goal of this study was to explore the influence of cross-sectional type, stacking sequence, and a variety of geometric

Presented as Paper 88-2251 at the AIAA 29th Structures, Structural Dynamics, and Materials Conference, Williamsburg, VA, April 18-20, 1988; received June 11, 1990; revision received Dec. 18, 1990; accepted for publication Dec. 26, 1990.

*Mechanical Engineer.
†Associate Professor, Aerospace and Ocean Engineering Department. Member AIAA.
‡Head, Aircraft Structures Branch, Structural Mechanics Division. Associate Fellow AIAA.

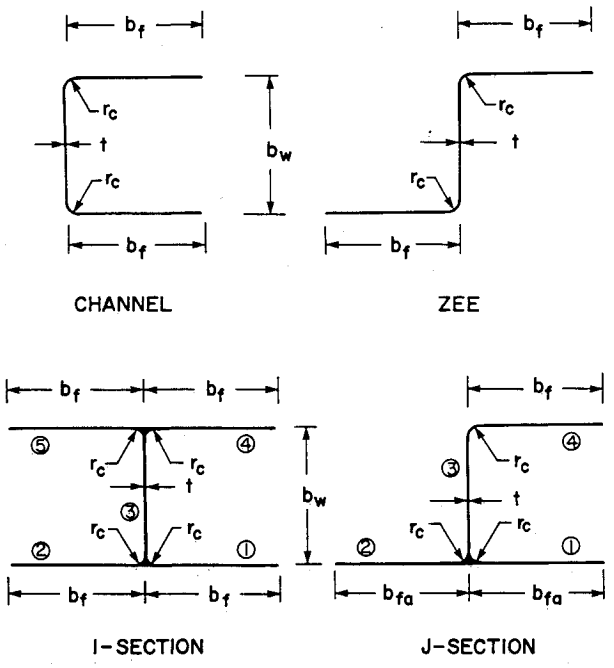

Fig. 1 Specimen cross sections and geometric parameters.

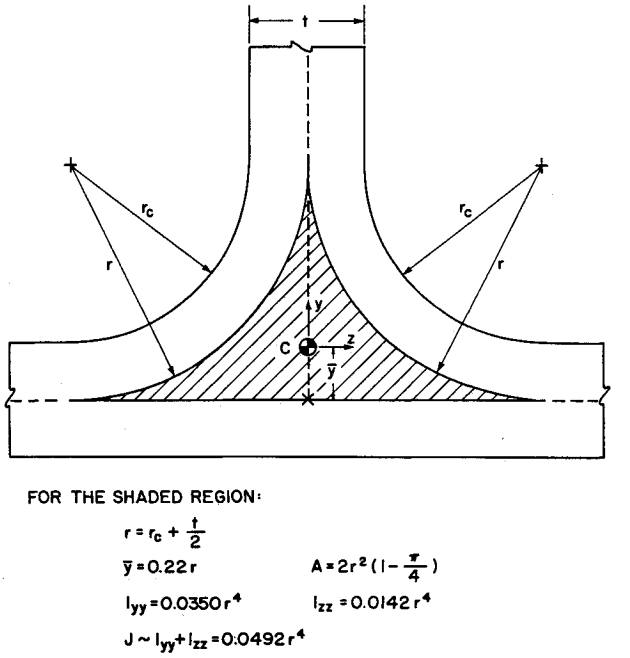

Fig. 2 Detail of filled corner region of I- and J-section specimens.

parameters on the buckling, postbuckling, and crippling response of stiffener specimens made from AS4/3502 graphite-epoxy material. The finite element shell analysis code STAGS[15] (STructural Analysis of General Shells) was used to create computational models for the full range of response of selected test specimens.

Specimens, Apparatus, and Tests

Thirty-six specimens with either channel, zee, I, or J cross sections and made from Hercules Inc. AS4/3502 graphite-epoxy unidirectional tape were tested during the current study. The nominal properties for this material system are E_1 = 127.5 GPa, E_2 = 11.31 GPa, G_{12} = 6.0 GPa, ν_{12} = 0.30, and ply thickness t_{ply} = 0.127 mm. The relevant geometric parameters associated with each cross section are shown in Fig. 1, where b_f is the flange width, b_{fa} is the attachment flange width (defined only for the J-section specimens), b_w is the web width, r_c is the inner corner radius, and t is the wall thickness. An idealized cross-sectional detail of those corner regions in the I- and J-section specimens where two coplanar flanges join the web is shown in Fig. 2. The shaded region in this figure is, in the physical specimens, filled by a rod of rolled unidirectional tape oriented axially along the specimen length. The nominal geometric parameters for each specimen are listed in Table 1. Because of the relatively large number of channel and zee specimens that have been tested in the past (e.g., Refs. 2, 5–7, 10, and 11), only three specimens of this type were tested as a part of the present work, and the discussion in this paper will concentrate on the I- and J-section specimens. As may be observed from Table 1, two different flange widths, two values of r_c, and three different symmetric layups were used to generate a variety of I and J cross sections. The layup designated L8 is an eight-ply quasi-isotropic stacking sequence $[\pm 45/0/90]_s$. Layup L16A is a 16-ply quasi-isotropic laminate $[\pm 45/0/90]_{2s}$, which doubles L8, and L16B denotes the 16-ply layup $[\pm 45/\mp 45/90/0_3]_s$, which produces orthotropic properties. The web width for all specimens and the attachment flange width for the J-section specimens were a constant 3.175 cm. According to the traditional local buckling analysis of stiffeners,[16] the relatively large value of the ratio b_f/b_w for the I- and J-section specimens in Table 1 implies that the flange elements will buckle before the web elements.

All specimens were cut from longer stiffeners fabricated by the Lockheed-Georgia Company under NASA Contract NAS1-15949. After any necessary machining of the flanges were performed to achieve the desired cross-sectional geometry, the ends of each specimen were embedded in an aluminum-epoxy potting compound to a depth of approximately 2.54 cm. The liquid potting compound was contained within a steel or aluminum ring. After the potting compound cured, the potted ends of the specimen were ground flat and parallel. This potting and grinding procedure provided for uniform load introduction during the testing of each specimen, and prevented end brooming failures. Several machined and potted specimens are shown in Fig. 3. The unsupported length l of each specimen (i.e., the length of the specimen between the potted ends) is given in the last column of Table 1. These lengths were chosen to avoid Euler column buckling, and were determined through bifurcation buckling analyses performed with the STAGS computer code.

Many electrical-resistance strain gages were applied to each specimen, typically in back-to-back pairs, to measure axial and lateral strains. Gages were installed in the corners, on the web, and on the flanges at axial locations corresponding to wave crests of the buckling modes as determined from the STAGS analysis. Direct-current displacement transducers (DCDTs) were used to monitor out-of-plane deflections of flanges and webs at selected locations, and a DCDT was also used to record load platen travel (specimen end shortening) during each test. Moiré interferometry provided a real-time qualitative measure of the buckling mode shape of a selected surface of each specimen during testing. Specimens were loaded in compression at a slow rate in a 1.33 MN hydraulic test machine. Data were recorded automatically every 2s during each test. The majority of the specimens were loaded to failure.

Analysis

The general shell-analysis computer code STAGS was used to perform geometrically nonlinear analyses of specimens I2, I10, I16, and Z1 from the current study, and of specimen Z6 from the work of Ref. 7 (designated specimen 1-15 in Ref. 7). The STAGS code is based on a shell theory that uses the Kirchhoff hypotheses, and neglects through-the-thickness extensional and shear strains, and thus interlaminar stresses. The 411 element from the STAGS finite element library, which has 12 out-of-plane and 20 in-plane degrees of freedom, was used in all analyses.

Table 1 Test specimens

Specimen designation[a]	Cross section	Flange width b_f, cm	Corner radius r_c, mm	Layup[b]	Gage length l, cm
I1	I	3.175	3.175	L8	10.16
I2	I	3.175	3.175	L8	15.24
I3	I	3.175	3.175	L8	30.48
I4	I	1.905	3.175	L8	10.16
I5	I	1.905	3.175	L8	20.32
I6	I	3.175	6.350	L8	10.16
I7	I	3.175	6.350	L8	20.32
I8	I	1.905	6.350	L8	10.16
I9	I	1.905	6.350	L8	20.32
I10	I	3.175	3.175	L16A	10.16
I11	I	3.175	3.175	L16A	20.32
I12	I	3.175	3.175	L16A	30.48
I13	I	1.905	3.175	L16A	10.16
I14	I	1.905	3.175	L16A	20.32
I15	I	3.175	3.175	L16B	10.16
I16	I	3.175	3.175	L16B	20.32
I17	I	3.175	3.175	L16B	30.48
I18	I	1.905	3.175	L16B	10.16
I19	I	1.905	3.175	L16B	20.32
J1	J	3.175	3.175	L8	10.16
J2	J	3.175	3.175	L8	20.32
J3	J	3.175	3.175	L8	30.48
J4	J	1.905	3.175	L8	10.16
J5	J	1.905	3.175	L8	20.32
J6	J	3.175	6.350	L8	10.16
J7	J	3.175	6.350	L8	20.32
J8	J	1.905	6.350	L8	10.16
J9	J	1.905	6.350	L8	20.32
J10	J	3.175	3.175	L16A	10.16
J11	J	3.175	3.175	L16A	20.32
J12	J	3.175	3.175	L16A	30.48
J13	J	1.905	3.175	L16A	10.16
J14	J	1.905	3.175	L16A	20.32
C1	Channel	1.270	3.175	L8	10.16
C2	Channel	1.270	3.175	L8	20.32
Z1	Zee	3.175	3.175	L16A	40.13
Z6[c]	Zee	3.175	3.175	L16A	10.16

[a]All specimens have a web width b_w of 3.175 cm, and are made from AS4/3502 graphite-epoxy.
[b]Layup L8 denotes $[\pm 45/0/90]_s$, layup L16A denotes $[\pm 45/0/90]_{2s}$, and layup L16B refers to $[\pm 45/\mp 45/90/0_3]_s$.
[c]Tested in Ref. 7 and designated specimen I-15 there.

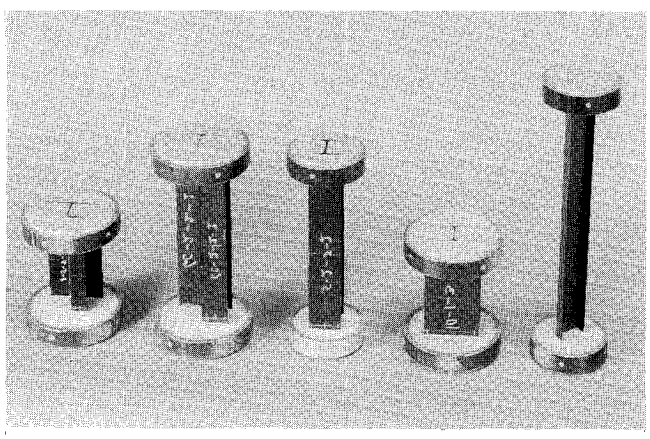

Fig. 3 Photograph of some specimens prepared for testing.

Results and Discussion

Experimental Results

Most of the I- and J-section specimens tested in the present study (see Table 1) had the same postcrippling appearance as the specimens examined in Ref. 7. As shown in Fig. 4, these specimens exhibited significant cross-sectional cracking (including broken fibers) at a certain axial location, accompanied by delaminations involving only one or a few ply interfaces at the free edges of the flanges. Specimens I15–I17, J10, J11, J13, and J14, however, exhibited a crippling failure that involved the delamination of only one ply interface and no broken fibers or matrix cracks. This delamination extended over a large portion of the specimen length and completely across the width of each pair of coplanar flanges, as shown by specimen I17 in Fig. 5. For specimens I13, I14, I18, and I19, buckling and failure were virtually simultaneous. These four failed specimens exhibited delaminations involving many ply interfaces that occupied only a small portion of the specimens' length, combined with a significant number of broken fibers (see Fig. 6), which is typical of a material compressive strength failure.

A summary of experimental results is presented for the I-section specimens in Table 2, and for the J-section specimens in Table 3. The inner corner radius r_c for each specimen is repeated from Table 1 for convenience. Tables 2 and 3 also list the flange width-to-thickness ratios $(b/t)_f$ for each specimen, where

$$(b/t)_f = \frac{(b_f - r_c - t/2)}{t} = \frac{b_f}{t} = \frac{r_c}{t} - \frac{1}{2}$$

The flange width-to-thickness ratio, as may be seen from Fig. 1, is the ratio of the width to the thickness of that part of a flange which may be considered a flat plate. The width-to-thickness ratio is identical for the four flanges of each I-section specimen under investigation. For the J-section specimens, the width-to-thickness ratio of the cap flange (denoted element 4 in Fig. 1) may be different from the $(b/t)_f$ ratio of the two attachment flanges. Tables 2 and 3 also give the

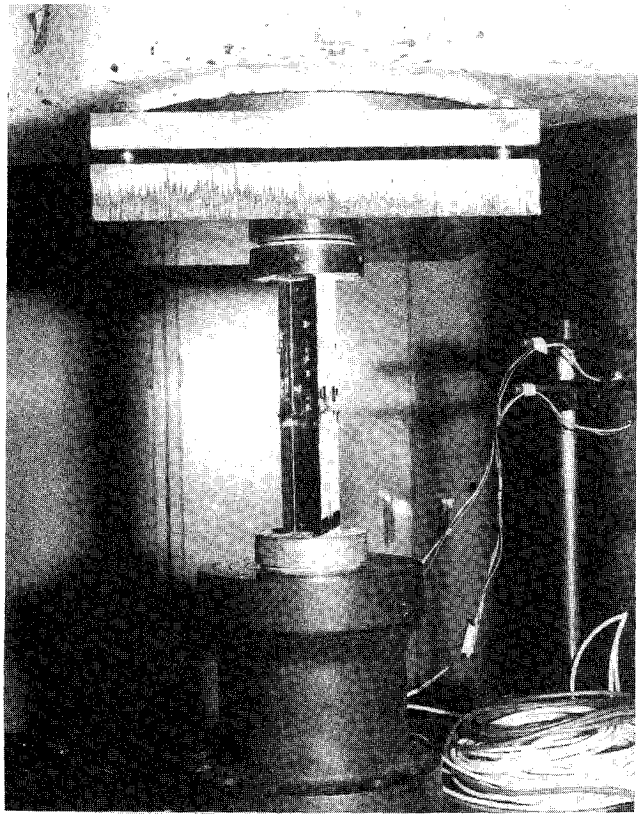

Fig. 4 Photograph of the crippling failure mode of specimen I5.

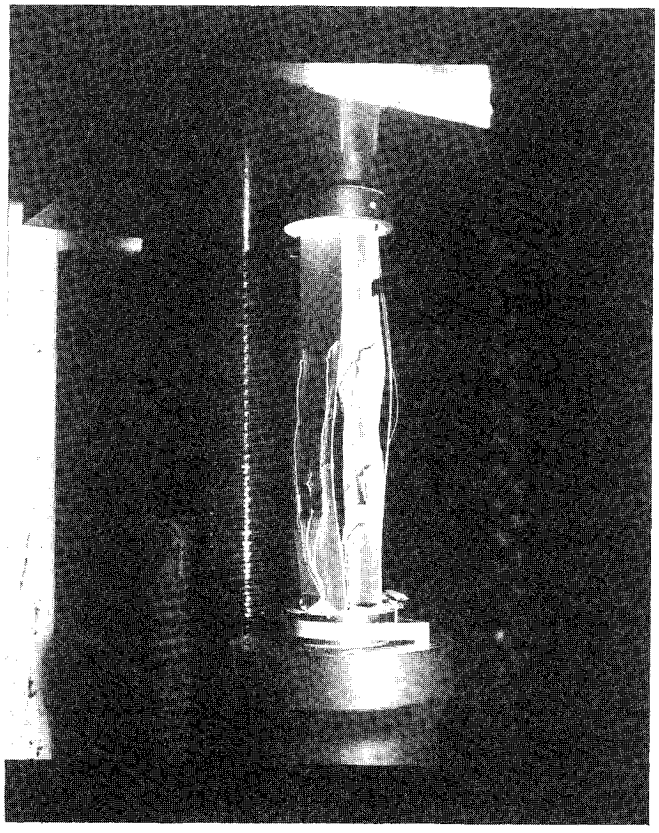

Fig. 5 Photograph of the crippling-failure mode of specimen I17. This mode exhibits a major delamination of one ply interface through the width of each pair of coplanar flanges.

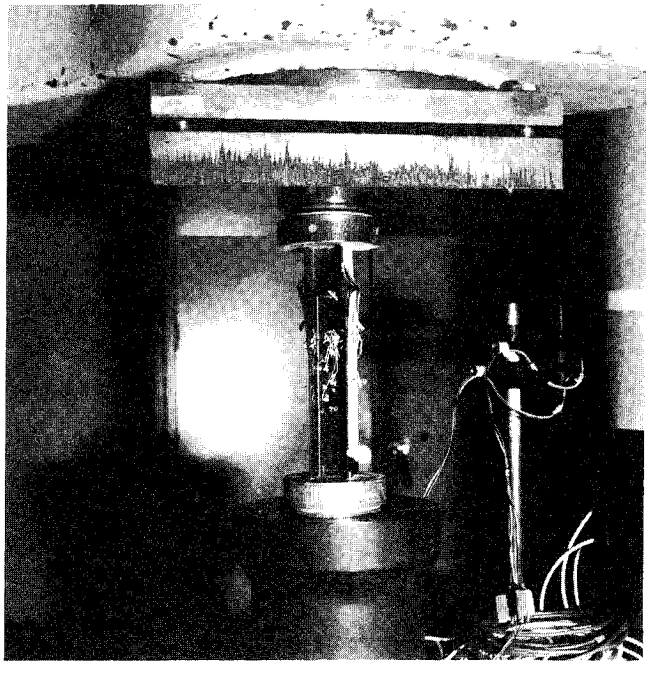

Fig. 6 Photograph of a material compressive-strength failure mode of specimen I14.

buckling load P_{cr} and crippling load P_{cc} for each specimen. For many of the J-section specimens, the cap flange has a significantly different buckling load than the attachment flanges. Such behavior was caused by 1) different $(b/t)_f$ ratios for the cap and attachment flanges, in which case different cap and attachment flange buckling modes were often also observed, and 2) the difference in rotational restraint at the junction with the web for the cap flange as compared to the attachment flanges. The buckling and crippling stresses, σ_{cr} and σ_{cc}, respectively, were obtained by dividing the appropriate load by the initial cross-sectional area of the specimen. The last column of Tables 2 and 3 contains an estimate of the location and nature of the first major damage event that occurred during the testing of each specimen. This estimate is based upon a detailed study[12] of all of the strain gage and DCDT data gathered during each test, and does not necessarily imply that crippling failure of the specimen was due to the same mechanism.

There are two important relationships that may be observed from the data in Tables 2 and 3. The first relationship involves the flange width-to-thickness ratio $(b/t)_f$ and the damage-initiation mode. For the five I-section specimens in Table 2 for which $(b/t)_f \geq 20$ (I1–I3, I6, and I7), damage initiation in a corner due to local compressive strength failure occurred for three of the specimens. Although the trend is not as clear for the J-section specimens in Table 3, the statement may again be made that for specimens in which all flanges have $(b/t)_f \geq 20$ (J1–J3, J6, and J7), damage seems more likely to initiate in a corner. Delamination at some point in a flange is the mode of damage initiation for those I- section specimens that have $10 \leq (b/t)_f \leq 20$ (I4, I5, I8, I9, I10–I12, and I15–I17). Apparently, flanges with a width-to-thickness ratio between 10 and 20 are more susceptible to delamination than are wider, thinner flanges. This observation is further reinforced by the damage-initiation modes of specimens J4, J5, J8, and J9, in which the attachment flange width-to-thickness ratios are greater than 20, but the cap flanges have $10 \leq (b/t)_f \leq 20$. Specimens J5 and J9 exhibited no precrippling damage events, but damage began in a cap flange delamination mode in both specimens J4 and J8. For specimens J10–J12, which have $10 \leq (b/t)_f \leq 20$ in all flanges, damage seemed to initiate as an attachment flange delamination in every case. For the I- and J-section specimens of the current investigation, flanges that have a width-to-thickness ratio less than about ten were resistant to buckling. (As noted above, specimens I13, I14, I18, and I19, which all have $(b/t)_f = 7.3$, buckled

Table 2 I-section experimental results

Specimen designation	Corner radius r_c, mm	$(b/t)_f^a$	Buckling Load P_{cr}, kN	Buckling Stress[b] σ_{cr}, MPa	Crippling Load P_{cc}, kN	Crippling Stress[b] σ_{cc}, MPa	Damage-initiation mode[c]
I1	3.175	27.625	13.34	79.01	45.347	268.5	N
I2	3.175	27.625	12.39	73.36	45.765	271.0	C
I3	3.175	27.625	11.12	65.84	43.372	256.8	C
I4	3.175	15.125	23.53	200.6	35.43	302.1	FD
I5	3.175	15.125	23.53	200.6	36.67	312.7	FD
I6	6.350	24.500	26.20	134.4	84.383	433.0	C
I7	6.350	24.500	21.62	110.9	89.431	458.8	FD
I8	6.350	12.000	52.086	363.5	60.929	425.2	D
I9	6.350	12.000	52.753	368.2	64.652	451.2	FD
I10	3.175	13.563	75.060	229.4	99.969	305.6	FD
I11[d]	3.175	13.563	64.656	197.7	—	—	DC
I12	3.175	13.563	62.588	191.3	92.403	282.5	D
I13	3.175	7.3125	118.81	530.7	121.39	542.2	C[e]
I14	3.175	7.3125	118.18	527.9	118.34	528.6	N
I15	3.175	13.563	81.016	247.7	87.461	267.4	D
I16	3.175	13.563	73.552	224.9	79.166	242.1	D
I17	3.175	13.563	69.580	212.7	75.883	232.0	D
I18	3.175	7.3125	134.73	601.8	137.33	613.4	N
I19	3.175	7.3125	125.39	560.1	125.40	560.1	N

[a]Flange width-to-thickness ratio.
[b]Average axial stress, defined as the compressive load divided by the original cross-sectional area.
[c]This column refers to the suspected nature and location of the first major damage event within the specimen as inferred from experimental data: C: corner damage due to local compressive material strength failure; FD: delamination in flange at free edge; DC: delamination in flange at corner; D: delamination initiating at a location that could not be determined; and N: no damage observed prior to failure.
[d]Test was stopped prior to failure so that the specimen could be c-scanned.
[e]Damage occurred prior to buckling at an axial strain level of approximately -9000 $\mu\varepsilon$. Very little evidence of further damage in postbuckling was found.

Table 3 J-section experimental results

Specimen designation[a]	Corner radius r_c, mm	$(b/t)_f^b$	Buckling Load P_{cr}, kN	Buckling Stress[c] σ_{cr}, MPa	Crippling Load P_{cc}, kN	Crippling Stress[c] σ_{cc}, MPa	Damage-initiation mode[d]
J1 A	3.175	27.625	7.864	59.9	34.35	261.8	N
C		27.625					
J2 A	3.175	27.625	8.451		32.03	244.1	U
C		27.625	7.117	54.3			
J3 A	3.175	27.625	8.362		28.18	214.8	CC
C		27.625	5.960	45.4			
J4 A	3.175	27.625	7.962	67.3	27.81	235.0	CFD
C		15.125	14.06				
J5 A	3.175	27.625	7.161	60.5	25.88	218.7	N
C		15.125	12.23				
J6 A	6.350	24.500	19.22		54.63	382.4	AC
C		24.500	15.26	106.8			
J7 A	6.350	24.500	14.95		49.67	347.7	CFD
C		24.500	13.66	95.63			
J8 A	6.350	24.500	19.39	149.3	41.52	319.6	CFD
C		12.000	28.29				
J9 A	6.350	24.500	18.90	145.5	35.40	272.4	N
C		12.000	29.85				
J10 A	3.175	13.563	56.792		70.98	276.6	AFD
C		13.563	54.01	210.5			
J11 A	3.175	13.563	49.208	191.7	58.94	229.7	AFD
C		13.563					
J12 A	3.175	13.563	48.13	187.5	58.94	229.7	AFD
C		13.563					
J13 A	3.175	13.563	51.15	221.6	64.496	279.4	AFD
C		7.3125					
J14 A	3.175	13.563		204.4	63.66	275.8	U
C		7.3125	48.193				

[a]Each specimen has two rows of information. The row marked "A" contains data for the attachment flanges in particular as well as global column information such as P_{cc}, σ_{cc}, and damage-initiation mode. The row marked "C" contains width-to-thickness ratio information for the cap flange, and buckling data for this flange if it is different from that for the attachment flanges.
[b]Flange width-to-thickness ratio.
[c]Average axial stress, defined as the compressive load divided by the original cross-sectional area. The buckling stress shown corresponds to the lowest flange buckling load for the specimen.
[d]This column refers to the suspected nature and location of the first major damage event within the specimen as inferred from experimental data: CC: corner damage at web-cap flange junction; AC: corner damage at web-attachment flange junction; CFD: cap flange free edge delamination; AFD: attachment flange free edge delamination; U: location and nature of damage uncertain; and N: no damage observed prior to failure.

and failed almost simultaneously.) This buckling resistance for small width-to-thickness ratio flanges suggests why damage initiated in an attachment flange for specimen J13 in Table 3, and not in the narrower cap flange of the section.

The second important relationship indicated from the data in Tables 2 and 3 involves the inner corner radius and the buckling and crippling stresses σ_{cr} and σ_{cc}. By comparing the σ_{cr} and σ_{cc} of specimens I1–I3 to I6 and I7, I4 and I5 to I8 and I9, J1–J3 to J6 and J7, and J4 and J5 to J8 and J9, the effect of increases r_c becomes clear. Each of these comparisons involves specimens whose cross sections are identical except for the inner corner radii. Increases in the buckling stress of 75–100% and in the crippling stress of about 50% occur for a doubling of the inner corner radius of these I- and J-section specimens. Such a consistent and substantial increase in stress for a doubling of r_c was not observed for the channel and zee specimens of Ref. 7. In I- and J-section stiffeners there are corners at which three cross-sectional elements (two flanges and the web) meet, which requires the insertion of unidirectional filler material during fabrication, as shown in Fig. 2. An increase in r_c implies an increase in the amount of filler material used. Only two cross-sectional elements meet at each corner of a channel or zee section, and consequently no corner filler material is necessary. Since an increased inner corner radius for the channel and zee specimens did not significantly increase the buckling or crippling stress, but an increased radius for the I- and J-section specimens did increase these stresses, the added corner filler material required by an increase in r_c is the most likely reason for the behavior of the I- and J-section specimens.

Analytical Results

The buckling loads obtained from experiment, STAGS bifurcation analysis, and STAGS nonlinear analysis are presented in Table 4 for specimens Z1, I2, I10, and I16 from the current study, and for specimen Z6 from Ref. 7. The percent errors in the analytical loads relative to the experimental buckling loads are also tabulated. For each specimen, the model used for the nonlinear analysis was derived by adding small initial geometric imperfections to the model used to obtain the bifurcation buckling load reported in Table 4. Although no bifurcation occurred in the nonlinear analysis, the buckling load was estimated from load-shortening plots and load vs back-to-back axial strain plots, as would be done with test data. As expected, the presence of these initial imperfections produces a buckling load below the bifurcation load in every case. The bifurcation buckling loads correlate fairly well with the experimental data. Agreement between the buckling loads obtained from experiment and nonlinear analysis is excellent.

The response of specimen I2 will serve to illustrate in detail the correlation between experiment and nonlinear STAGS analysis. The finite element model of this specimen consists of five plates (four flanges and the web). At each of the two corners, two flange plates and the plate representing the web meet at initially right angles. The 0-deg fiber-filled corner regions detailed in Fig. 2 are modeled as discrete beam columns having the same cross-sectional properties as the shaded area in the figure. The model is shown in a buckled state in Fig. 7 (the beam columns do not appear in this STAGS deformed geometry plot). The portions of the specimen embedded in the potting compound are included at each end of the model to account for the axial deformation of the specimen embedded in the potting material. For the line of nodes located where the potting material ends and the exposed specimen begins, the out-of-plane displacement, lateral in-plane displacement, and out-of-plane rotation normal to the potting were specified to vanish. The axial displacement and remaining rotations were free.

Load-shortening curves for specimen I2 are shown in Fig. 8, where the solid line denotes the results of the STAGS

Table 4 Experimental and analytical buckling loads

Specimen designation	Experimental buckling load, kN	Analytical buckling load, kN[a]	
		Bifurcation analysis	Nonlinear analysis
Z1	31.49	35.31 (12.1%)	33.62 (6.8%)
Z6[b]	37.36	42.47 (13.7%)	36.92 (−1.2%)
I2	12.39	13.79 (11.3%)	12.90 (4.1%)
I10	75.06	73.51 (−2.1%)	71.72 (−4.4%)
I16	73.55	79.79 (8.5%)	75.84 (3.1%)

[a]Percent error with respect to experimental buckling load is given in parentheses.
[b]Tested in Ref. 7.

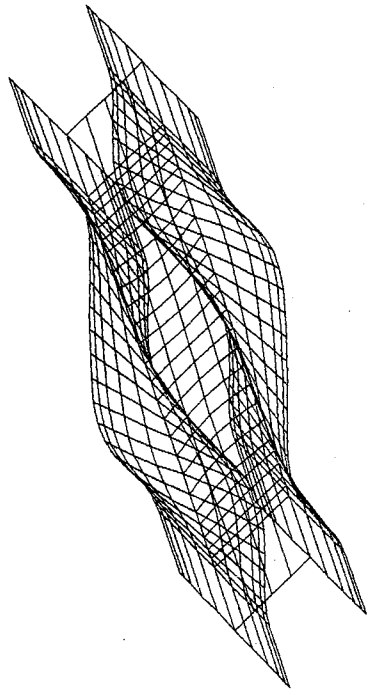

Fig. 7 Buckling mode of specimen I2 from STAGS bifurcation analysis.

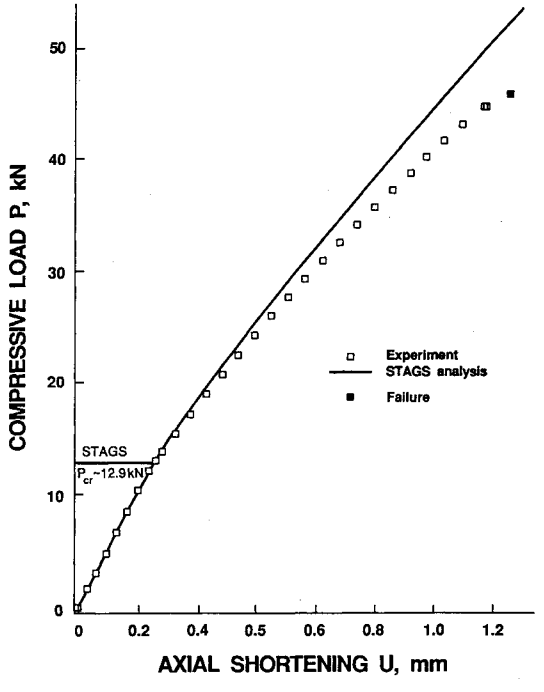

Fig. 8 Experimental and analytical load-shortening data for specimen I2.

analysis and the open squares represent experimental data. The filled square indicates failure (crippling). The correlation between experimental and analytical results for this global measure of specimen response is excellent prior to and through buckling, and the correlation remains good over a significant range of the postbuckled region. A more local measure of the agreement between analysis and experiment for specimen I2 may be realized from the cross-sectional distributions of axial surface strain presented in Figs. 9 and 10. Analytical and experimental strains near the experimental buckling load and at an axial position of $l/3$ are plotted vs a piecewise continuous contour coordinate in Fig. 9. The vertical dashed lines denote divisions between the five plate elements of the STAGS model. The correlation is excellent at this load, and is even better at lower loads, where a uniform distribution of axial strain exists. The axial strains for specimen I2 at the crippling load, P = 45.765 kN, are shown in Fig. 10. The agreement between experiment and analysis is diminished at this load. The most likely reasons for the degradation of correlation in postbuckling observed in Figs. 8 and 10 include a damage event that occurred at a load of 44.480 kN during the testing of specimen I2, the neglect of transverse shear deformations by STAGS, and modeling deficiencies in the corners.

Failure Analysis

In-plane stress data in principal material coordinate directions were obtained from the STAGS analyses at the load corresponding to the first damage event for specimens Z1,

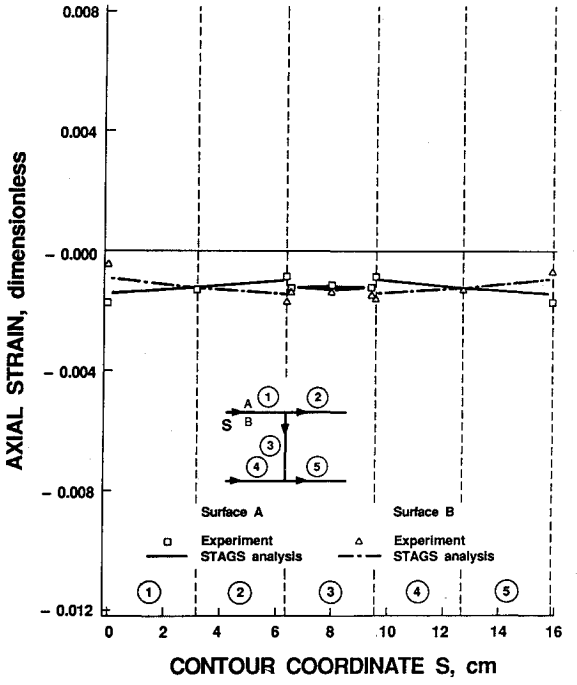

Fig. 9 Experimental and analytical axial surface strain distributions for specimen I2 at an axial position of $l/3$ and compressive load P = 12.33 kN (P/Pcr = 0.995).

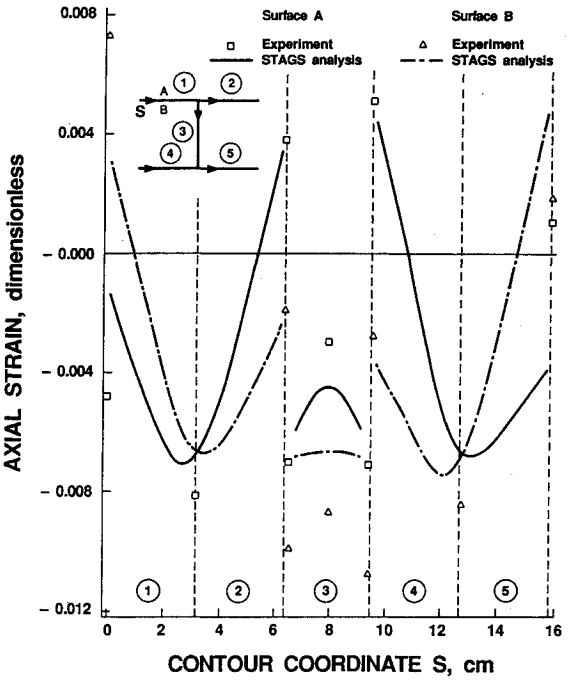

Fig. 10 Experimental and analytical axial surface strain distributions for specimen I2 at an axial position of $l/3$ and compressive load P = 45.765 kN (P/Pcr = 3.693).

Table 5 Results of plane stress failure analysis

Specimen designation	Load P, kN	Failure criterion[a]	Maximum value of criterion,[b] dimensionless	Ply orientation for maximum value,[c] deg	Location of maximum value
Z1	37.35	CFM	0.805	0	Corner
		CMM	0.544	45	Flange free edge
		THT	0.667	45	Flange free edge
Z6[d]	53.914	CFM	1.138	0	Corner
		CMM	0.935	45	Flange free edge
		THT	1.300	0	Corner
I2	44.480	CFM	1.348	0	Web near corner
		CMM	1.445	45	Web near corner
		THT	1.915	45	Web near corner
I10	83.400	CFM	0.881	0	Flange near corner
		CMM	0.583	45	Flange free edge
		THT	0.830	45	Flange free edge
I16	78.151	CFM	0.990	0	Entire flange
		CMM	0.940	45	Flange free edge
		THT	1.238	45	Flange free edge

[a]The failure criteria listed are CFM: Hashin's compressive-fiber mode failure criterion; CMM: Hashin's compressive-matrix mode failure criterion; and THT: Tsai-Hill failure criterion.
[b]The material strength parameters used are X_t = 1.45 GPa, X_c = −1.45 GPa, Y_t = 52.0 MPa, Y_c, = −206 MPa, and S = 93.1 MPa.
[c]Orientation of ply in which the maximum value of the criterion listed occurred.
[d]This specimen was tested in Ref. 7 and was analyzed at the crippling load. The failure analyses for the other specimens shown were performed at the load corresponding to the first damage event within each specimen.

I2, I10, and I16, and at the crippling load for specimen Z6. For shell elements near the axial location of failure in the specimen, stresses were computed at the top and bottom of each ply along the normals to the centroids of the elements. Six criteria specialized to the plane stress condition were investigated; the Tsai-Hill and Tsai-Wu (tensor polynomial) criteria, and the four failure criteria proposed by Hashin.[17] The Hashin criteria are the tensile-fiber compressive-fiber, tensile-matrix, and compressive-matrix modes. If X denotes a fiber-direction strength, Y a strength perpendicular to the fibers, S a shear strength, and subscripts t and c represent tension and compression, respectively, then the material strength parameters used in this failure analysis are $X_t = 1.45$ GPa, $X_c = -1.45$ GPa, $Y_t = 52.0$ MPa, $Y_c = 206$ MPa, and $S = 93.1$ MPa. These values were obtained from Ref. 18 for AS/3501 graphite-epoxy material and are representative of the AS4/3502 material system used in the current investigation.

The results of the plane stress failure analysis are given in Table 5. Only data for the compressive-fiber and compressive-matrix mode criteria of Hashin and for the Tsai-Hill criterion are presented, since the failure indices of the other three criteria were consistently well below 1.0 (For all of the criteria, a failure index of unity or greater implies failure.) The maximum value of each criterion, the orientation of the ply in which the maximum occurred, and the cross-sectional location of this maximum are listed. The generally nonconservative failure predictions obtained for specimens Z1, Z6, I10, and I16, all of which have a relatively small flange width-to-thickness ratio of 13.6, are likely due to the lack of interlaminar stress data, and thus an inability to evaluate delamination failures. (As discussed previously, experimental evidence suggests that damage initiates in a delamination mode caused by bending in flanges with $10 \leq (b/t)_f \leq 20$.) In the absence of interlaminar stress information, the compressive-fiber mode criterion of Hashin seems to correlate best with experimental damage initiation. This criterion is $\sigma_{11}/X_c = 1$, where σ_{11} is the compressive stress in the fiber direction, and is in fact simply a maximum fiber-direction compressive-stress criterion.

Concluding Remarks

Two crippling-failure modes have been observed for the I- and J-section stiffener specimens in this study. The first mode consists of a crack across the entire cross section accompanied by flange free-edge delaminations involving only one or a few ply interfaces. Broken fibers are visible in this crippling mode. (This crippling failure mode was also observed for the channel and zee specimens in Ref. 7 and in the present study.) The second mode is characterized by a delamination of a single interface that extends across the entire width of two coplanar flanges and over a substantial length of the specimen. No broken fibers are visible.

For the I- and J-section specimens considered in the current investigation, the flange width-to-thickness ratio has been found to influence the initiation of damage. For a flange with $10 \leq (b/t)_f \leq 20$, damage seems likely to initiate in that flange as a result of delamination due to bending. For a flange with $(b/t)_f \geq 20$, damage appears to begin in some other cross-sectional location, either in a corner due to a local compressive strength failure or in a different flange with $10 \leq (b/t)_f \leq 20$. Sixteen-ply I-section specimens with $(b/t)_f = 7.3$ in all flanges exhibited little or no postbuckling response prior to failure, and had very high strains at failure. The failure mode of these specimens appeared to be a local material compressive strength failure, in which many ply interfaces delaminated across the entire width of each pair of coplanar flanges. The damage was confined to a small portion of the axial length, and many broken fibers were visible.

Increasing the inner corner radius r_c of the I- and J-section specimens from 3.175 mm to 6.350 mm has been found to produce a significant increase in the average buckling and crippling stresses. Such an increase in r_c allows more unidirectional filler material to be inserted in the corner regions of these specimens, and thus appears to be an efficient way to improve substantially the performance of these stiffener sections. However, the same increase in r_c for the channel and zee specimens of Ref. 7 did not significantly increase either the buckling or crippling stresses because no filler material is required at the corners.

Analyses of the geometrically nonlinear response of specimens Z1, I2, I10, and I16 from the current study and specimen Z6 from Ref. 7 have been performed using the STAGS computer code. The correlation between experimental and analytical results is excellent prior to and at buckling, and in the initial postbuckling response. Correlation degrades in postbuckling because of damage that occurred in the buckled specimens during testing, the influence of transverse shearing deformations neglected in the analysis, and limitations on the modeling of the filled I- and J-section corner regions. These factors cause the analyses to exhibit greater load-carrying capacity during postbuckling than was experimentally observed.

Using in-plane stress data obtained from the STAGS analyses at the load corresponding to the first observed damage event for each analyzed specimen, it has been found that the maximum compressive-stress criterion in the fiber direction correlates reasonably well with experimental observations of damage initiation. Similarly, Arnold and Mayers[13] found that the maximum compressive-fiber strain criterion yields a reasonable estimate of the crippling load for no-edge-free plates. However, the inability to determine interlaminar stresses in the current analysis precludes an evaluation of the initiation of crippling failure by delamination. Delamination may initiate at the free edges of the flanges due to bending, or may initiate in the interior of a pair of coplanar flanges near the junction with the web where the stiff unidirectional insert is located.

Acknowledgment

This work was sponsored in part by the NASA Langley Research Center under Grants NAG1-343 (NASA-Virginia Tech Composites Program) and NAG1-537.

References

[1]Spier, E. E., "Crippling/Column Buckling Analysis and Test of Graphite/Epoxy Stiffened Panels," AIAA Paper 75-753, May 1975.

[2]Spier, E. E., and Klouman, F. L., "Empirical Crippling Analysis of Graphite/Epoxy Laminated Plates," *Composite Materials: Testing and Design* (Fourth Conf.), ASTM STP 617, American Society for Testing and Materials, 1977, pp. 255–271.

[3]Spier, E. E., "Stability of Graphite/Epoxy Structures with Arbitrary Symmetrical Laminates," *Experimental Mechanics*, Vol. 18, No. 11, Nov. 1978, pp. 401–408.

[4]Spier, E. E., "On Experimental Versus Theoretical Incipient Buckling of Narrow Graphite/Epoxy Plates in Compression," *Proceedings of the AIAA/ASME/ASCE/AHS 21st Structures, Structural Dynamics, and Materials Conference*, AIAA, New York, 1980, pp. 187–193.

[5]Spier, E. E., "Postbuckling Fatigue Behavior of Graphite-Epoxy Stiffeners," *Proceedings of the AIAA/ASME/ASCE/ASH 23rd Structures, Structural Dynamics, and Materials Conference*, Part 1, AIAA, New York, 1982, pp. 511–527.

[6]Spier, E. E., Arnold, R. R., and Kedward, K. T., "Stability Critical Compression Members," *Handbook of Composites, Vol. 2—Structures and Design*, edited by C. T. Herakovich and Y. M. Tarnopol'skii, Elsevier, Amsterdam, 1989, pp. 583–622.

[7]Tyahla, S. T., and Johnson, E. R., "Failure and Crippling of Graphite-Epoxy Stiffeners Loaded in Compression," Rept. CCMS-84-07 and VPI-E-84-19, Center for Composite Materials and Structures, Virginia Polytechnic Inst. and State Univ., Blacksburg, VA, June 1984.

[8]Reddy, A. D., Rehfield, L. W., Bruttomesso, R. I., and Krebs, N. E., "Local Buckling and Crippling of Thin-Walled Composite Structures Under Axial Compression," *Proceedings of the AIAA/ASME/ASCE/AHS 26th Structures, Structural Dynamics, and Mate-*

rials Conference, Pt. 1, AIAA, New York, 1985, pp. 804–810.

[9]Rehfield, L. W., and Reddy, A. D., "Observations on Compressive Local Buckling, Postbuckling, and Crippling of Graphite/Epoxy Airframe Structure," *Proceedings of the AIAA/ASME/ASCE/AHS 27th Structures, Structural Dynamics, and Materials Conference*, Pt. 1, AIAA, New York, 1986, 301–306.

[10]Causbie, S. M., and Lagace, P. A., "Buckling and Final Failure of Graphite/PEEK Stiffener Sections," *Proceedings of the AIAA/ASME/ASCE/AHS 27th Structures, Structural Dynamics, and Materials Conference*, Pt. 1, AIAA, New York, pp. 280–287.

[11]Wang, C., Pian, T. H. H., Dugundji, J., and Lagace, P. A., "Analytical and Experimental Studies on the Buckling of Laminated Thin-Walled Structures," *Proceedings of the AIAA/ASME/ASCE/ASH 28th Structures, Structural Dynamics, and Materials Conference*, Pt. 1, AIAA, New York, 1987, pp. 135–140.

[12]Bonanni, D. L., Johnson, E. R., and Starnes, J. H., Jr., "Local Buckling and Crippling of Composite Stiffener Sections," Center for Composite Materials and Structures, Virginia Polytechnic Inst. and State Univ., Blacksburg, VA, Rept. CCMS-88-08 and VPI-E-88-15, June 1988.

[13]Arnold, R. R., and Mayers, J., "Buckling, Postbuckling and Crippling of Materially Nonlinear Laminated Composite Plates," *International Journal of Solids and Structures*, Vol. 20, No. 9/10, 1984, pp. 863–880.

[14]Starnes, J. H., Jr., Knight, N. F., Jr., and Rouse, M., "Postbuckling of Selected Flat Stiffened Graphite-Epoxy Panels Loaded in Compression," *Proceedings of the AIAA/ASME/ASCE/AHS 23rd Structures, Structural Dynamics, and Materials Conference*, Pt. 1, AIAA, New York, 1982, pp. 464–478.

[15]Almroth, B. O., Brogan, F. A., and Stanley, G. W., "User's Manual for STAGS," Lockheed Palo Alto Research Lab., CA, NASA Contractor Rept. 165670, Contract NAS1-10843, Vols. 1 and 2, March 1978.

[16]Becker, H., "Handbook of Structural Stability, Pt. II—Buckling of Composite Elements," NACA TN-3782, July 1957, p. 29.

[17]Hashin, Z., "Failure Criteria for Unidirectional Fiber Composites," *Journal of Applied Mechanics*, Vol. 47, No. 2, June 1980, pp. 329–334.

[18]Tsai, S. W., *Composites Design—1986*, Think Composites, Dayton, OH, 1986, p. 10-8.